Soils and Rocks
An International Journal of Geotechnical and Geoenvironmental Engineering
www.soilsandrocks.com
ISSN 1980-9743
ISSN-e 2675-5475

The 7th Bishop Lecture: The mechanics of coarse-grained geomaterials at meso- and micro-scales

Matthew Coop[1*]

Lecture

Keywords
Particle mechanics
Laboratory apparatus
Sands
Coarse-grained soils

Abstract

In order to move towards discrete analyses of soil behaviour, we need to develop a new range of apparatus and testing techniques. The lecture describes attempts to develop these new apparatus and presents data for a range of coarse-grained geomaterials at the single particle scale. The roles of the particle morphology and hence geological origin are discussed and are shown to influence both the contact mechanics and particle breakage behaviour. The mechanics of single particles are shown to be more complex than generally assumed and will require new means of modelling to account for the significant plasticity that occurs at particle contacts and patterns of breakage that are strongly influenced by the origins of particles and their effect on their morphology.

1. Introduction

Traditionally, coarse grained soils have been treated as continua using meso-scale laboratory tests such as the triaxial to derive ever more complicated constitutive models as newly discovered aspects of behaviour are included. Some of these are features that are shared with plastic soils, such as creep, rate of loading effects, anisotropy, the influence of stress rotation and of the intermediate principle stress, but others are more clearly related to the coarse grain size. While for a clay the initial depositional density only affects the behaviour at very low stress levels, for coarse grained soils this influence extends up to the onset of particle breakage when compression paths tend to converge to a unique normal compression line in the volumetric plane (Pestana & Whittle, 1995). This particle breakage has a number of consequences, for example that sands tend not to follow Rendulic's principle, the state boundary surface has an asymmetrical shape so that the flow-rule is non-associated and the stress history of a sand and the effect it has on breakage has an important influence on stiffness (e.g. Coop & Lee, 1993; Jovicic & Coop, 1997).

In the volumetric plane the critical state line for sands curves to a horizontal asymptote at low stresses (Verdugo & Ishihara, 1996) the higher gradients at larger stresses generally being attributed to the onset of breakage, even if it may be found in non-plastic soils with no apparent particle damage (e.g. Carrera et al., 2011). However, what seems to be a unique critical state line is affected by prior breakage (Muir Wood, 2008; Bandini & Coop, 2011) and continued shearing to strains well beyond what a triaxial can achieve reveals continued particle breakage (Coop et al., 2004). Some sands, for example when they are fractally graded or have particles of mixed mineralogies, may even have a transitional mode of behaviour in which the critical state line location in the volumetric plane becomes dependent on the initial density at deposition (e.g. Todisco & Coop, 2019). Added to each of these features of the behaviour of reconstituted sands are the influence of the natural fabric and bonding (Cuccovillo & Coop, 1999).

Considering also the practical difficulties of meso-scale tests on sands (e.g. particle size effects, membrane penetration, sample end restraint, strain localisation) one begins to wonder why we bother at all with continuum approaches. A discrete methodology starts to look attractive, for example using DEM. But often this is done with unrealistic particle shapes, such as spheres, and with unrealistic contact models. The normal loading behaviour at the contact is frequently assumed to be linear or following a non-linear Hertz (1882) model based on the contact of two elastic spheres. In lateral loading, the same linear stiffness as for normal loading is frequently assumed with a frictional sliding cut-off when the inter-particle coefficient of friction, μ, is reached, or at best the Mindlin & Deresiewicz (1953) extension of Hertz is used. A rolling resistance is often adopted to stop excessive rotation of the particles, but this is purely artificial and only needed because of the spheres adopted in simple models. Twisting at the contact is generally ignored and Zhai et al. (2019) have found that its effects are typically small.

Various techniques are available to model more realistic shapes such as potential particles (e.g. Ahmed et al., 2016) or using overlapping spheres (Fellerec & McDowell, 2010), which obviate the need for a rolling resistance, but it is still often the case that the input contact parameters are derived by curve fitting the DEM analyses to meso-scale laboratory

*Corresponding author: E-mail address: m.coop@ucl.ac.uk
[1]University College London, London, UK.

Submitted on May 30, 2023; Final Acceptance on November 20, 2023; Discussion open until November 30, 2024.
https://doi.org/10.28927/SR.2024.006723

test data (Ahmed et al., 2016). If we are to adopt a truly "micro" approach, the use of DEM should be accompanied by micro-scale tests to derive directly the particles shapes, their contact fabric and most importantly their contact mechanics as well as gaining an understanding of the occurrence and modes of particle damage. These will each require new techniques and the focus of this lecture will be the use of these new apparatus to examine the contact behaviour and damage of single particles.

2. Development of new apparatus

Previous work on the micro-mechanics of sand particles has typically used mechanical apparatus to determine inter-particle friction (Horn & Deere, 1962; Skinner, 1969; Procter & Barton, 1974) and particle strength has generally been measured in platen-to-platen loading (e.g. Nakata et al., 1999). Even recent work examining more detailed aspects of the contact mechanics has usually been in relatively simple apparatus examining one aspect of behaviour (e.g. Cole et al., 2010; Cole, 2015; Michalowski et al., 2018). Instead, the approach adopted here has been to develop a universal and computer-controlled apparatus capable of examining all aspects of loading under combined normal and tangential loading from the very small displacement stiffnesses up to failure, the equivalent of the stress path controlled triaxial apparatus for single particle contacts.

The apparatus developed are shown in Figure 1; one for sand sized grains built at the City University of Hong Kong and one for railway ballast or rock fill at University College London. Each has independent three axis control of the displacements and/or loads applied at the contact between two particles via linear actuators. The forces and displacements in each direction are measured by load cells and non-contacting displacement transducers, with precisions for the displacements to about ±0.01 μm and 0.01 N for the load on the larger apparatus which has a 1 kN capacity and about 0.001 N for the smaller one built for 100 N. One particle is mounted on an upper platen attached to the vertical load cell while the other is attached to a base pedestal mounted on a sled on a quasi-frictionless three-point bearing system. The systems were built for high rigidity to minimise any effect of apparatus compliance, especially at small displacements. Two microscope cameras monitor the particle contact from two orthogonal directions.

For the natural sands that have been tested the more spherical particles available have been chosen so that the local radius of curvature at the contact corresponds to that of the particle overall. But for materials such as ballast that are comprised of crushed rock this is not possible and typically a particle corner or point is tested against a nominal flat as in Figure 2. The cameras allow measurement of the local radius of curvature of the point for comparison with theoretical predictions of the contact stiffnesses.

This type of apparatus is suitable for testing frictional uncemented particles. It cannot measure rolling or twisting resistance, but as discussed above the former is largely fictitious for uncemented particles and the latter small. For cemented particles, however, the resistance to combined normal shear and moment loading must be measured and Figure 3 shows an apparatus developed at the City University of Hong Kong.

It is based on the apparatus in Figure 1 but applies the horizontal or shear loads through reaction arms, the height of which may be adjusted to give a moment. These

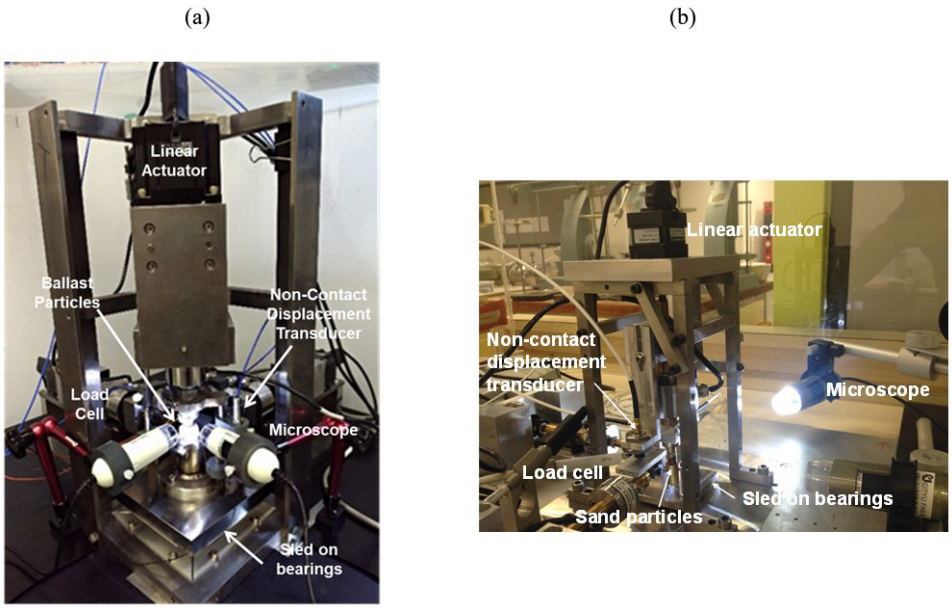

Figure 1. Inter-particle loading apparatus for: (a) ballast/rock fill; (b) sands.

act via a knife edge against L-shaped mounts that transfer the loads to the top and base of the cemented particle pair. The axial loads are applied to the mounts through pin joints. This style of loading system was used by Jiang et al. (2012) to investigate the contact behaviour of bonded artificial particles. The horizontal loading in this case is in 2D only and the displacements are measured by LVDTs, two being mounted one above the other in the horizontal direction so that the shear displacement and rotation can both be resolved.

To gain insight into the mechanisms of particle breakage a simplified version of the loading apparatus was constructed for vertical loading only that enabled high speed imagery of the tests (Figure 4) in which a microscope lens was attached to a high-speed camera.

3. Normal loading behaviour

Selected data for a variety of sands are given in Figure 5a. The Leighton Buzzard sand is a quartz sedimentary sand from Southeast England. The Philippines carbonate sand is biogenic in origin and the particles tested were selected to be solid coral fragments. The crushed limestone was an artificial sand created by crushing a young limestone from China, while the completely decomposed granite was from Hong Kong, and was created by weathering. The most spherical of the particles was tested in each case so that the sphericities assessed from the Krumbein & Sloss (1963) identification chart were all 0.7-0.8. They were all well rounded with values of roundness of 0.6-0.7 apart from the crushed limestone which had a mean roundness of 0.3 arising from the crushing process.

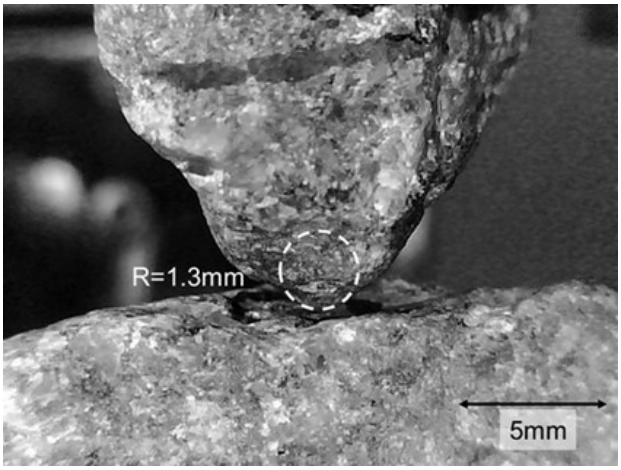

Figure 2. Point to flat contact for a railway ballast (after Wong & Coop, 2023).

All the data in Figure 5a are for particle sizes in the range 1.18−2.36 mm and to some extent the differences between the curves result from the variation of sizes. Also important though are any local shape variations at the contact, especially because of the low roundness of the crushed limestone and also the mineralogy that controls the Young's modulus of each material, E. Quartz has an E of around 94−98 GPa while for the calcite of the carbonate sand and crushed limestone E = 73−84 GPa (Mavko et al., 1998; Jaeger et al., 2007). The decomposed granite has a mixed mineralogy mostly of quartz and feldspar, but the main cause of its very soft contact behaviour is the coating of clay on the particles that results from the weathered origin. These large displacements were therefore mostly plastic and were also not generally present when the clay coating was washed off as can be seen in the data labelled WCDG on Figure 5b.

Most of the data on Figure 5b are for a granite railway ballast (Wong & Coop, 2023) supplied from the Mountsorrel quarry in the UK. Because of the very irregular shapes a nominal point was generally tested against a nominal flat, as in Figure 2, the contact radius of the point being derived from the microscope camera images. While there is little direct correlation between the contact radii that are indicated for each test on the figure, it is clear that the load-deflection curves are very much softer than for the contact of smooth spheres of gneiss tested by Cole et al. (2010) and are much closer to the contact behaviour of the much smaller Leighton Buzzard sand from Nardelli & Coop

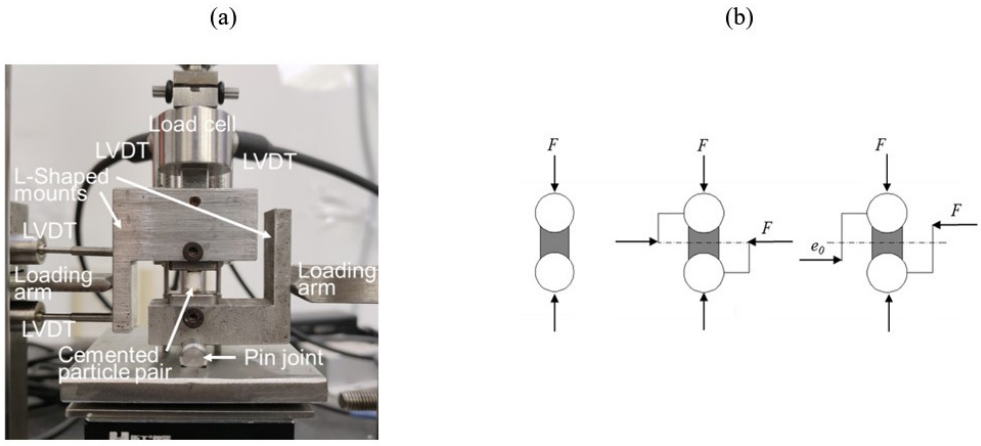

Figure 3. Inter-particle loading apparatus for cemented particles: (a) photo; (b) schematic (modified from Wang et al., 2019).

(2019). This is largely because the contact radii of the granite are more similar to the sand than the 14.7 mm diameter spheres Cole et al. (2010) used, but also probably because of the very high roughness of the ballast (mean S_q = 18.2 μm).

The simplest theory with which the data may be compared is that of Hertz (1882) which gives the mutual displacement δ at the contact of two elastic spheres:

$$\delta = \frac{a_H^2}{R} = \left(\frac{9N^2}{16RE^{*2}} \right)^{1/3} \quad (1)$$

where a_H is the radius of the contact area, R the equivalent radius ($1/R = 1/R_1 + 1/R_2$), N the normal force and E^* the equivalent Young's modulus, taken as $1/E^* = (1 - \nu_1^2)/E_1 + (1 - \nu_2^2)/E_2$ in which ν_1, E_1, ν_2 and E_2 are the Poisson's ratios and Young's moduli of the two contacting materials. The Poisson's ratio of quartz is 0.065−0.068 (Mavko et al., 1998; Jaeger et al., 2007). Hertz assumes that there are elastic strains in the vicinity of the contact but zero strain in the bulk of the particle.

To account for the roughness of the particles which increases the contact displacements Greenwood et al. (1984) defined a normalised roughness, α:

$$\alpha = \frac{\sigma R}{a_H^2} \quad (2)$$

where σ is the combined roughness of the two surfaces $\sigma = (S_q^2 + S_{q2}^2)^{1/2}$ in which S_{q1} and S_{q2} are the RMS roughnesses of the surfaces, which for the Leighton Buzzard sand was measured by white light interferometry to be 0.29 ± 0.09 μm (Nardelli & Coop, 2019). The apparent area of the contact between two rough surfaces is then a^* which replaces a_H in Equation 1 which, based on experimental data for metals, Yimsiri & Soga (2000) suggested could be given by:

$$\frac{a^*}{a_H} = \frac{-2.8}{\alpha + 2} + 2.4 \quad (3)$$

The Hertz predictions and those of "Hertz with roughness" are compared in Figure 6 with typical data for a pair of Leighton Buzzard sand particles. At low loads the roughness of the particles plays an important role and Hertz is far too stiff, while Hertz with roughness gives a perfect

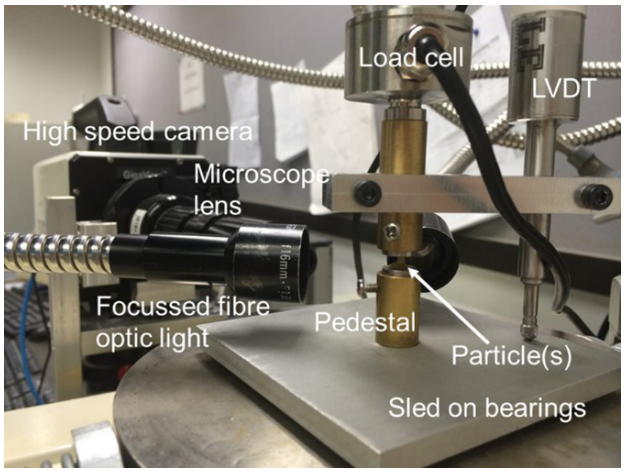

Figure 4. Particle crushing apparatus (modified from Todisco et al., 2017).

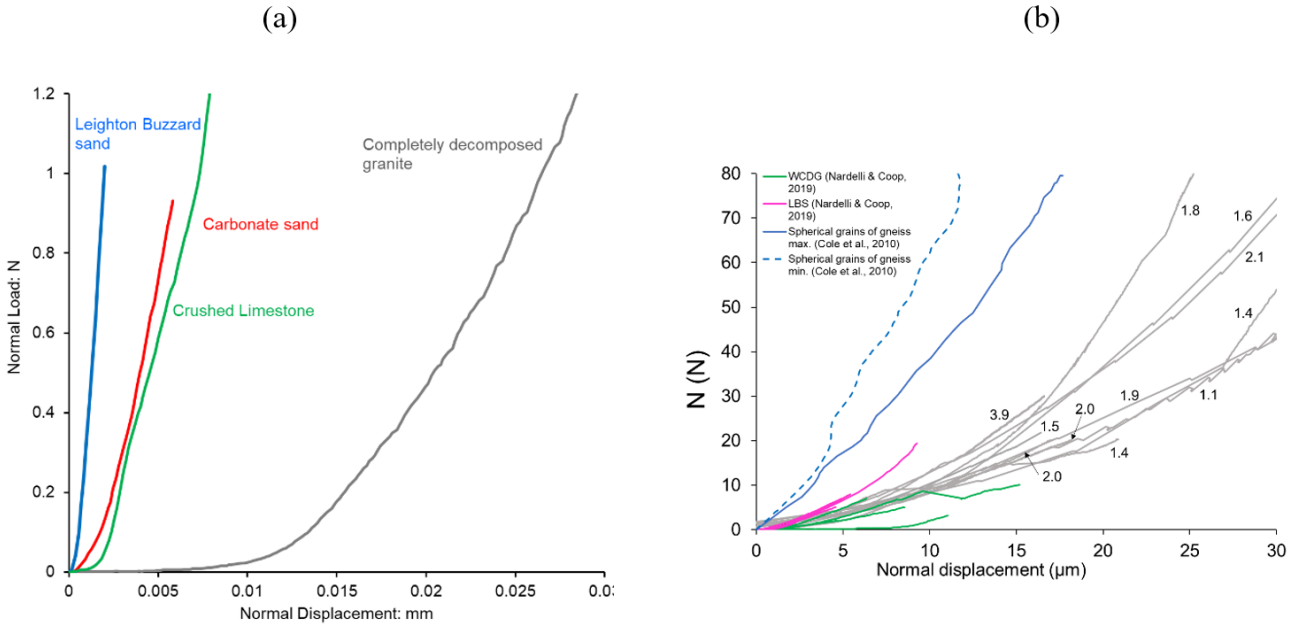

Figure 5. Normal loading behaviour of various materials: (a) sands (data from Nardelli & Coop, 2019); (b) granite ballast (after Wong & Coop, 2023).

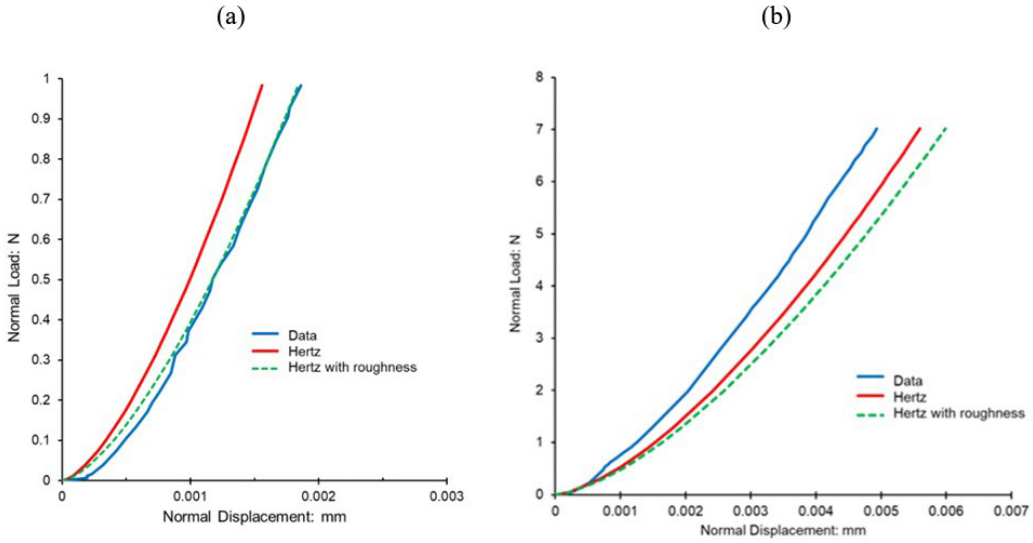

Figure 6. Comparisons between data for Leighton Buzzard sand and Hertz with and without roughness: (a) low loads; (b) higher loads; (modified from Nardelli & Coop, 2019).

fit. But at higher loads, presumably as the asperities flatten, the data show a behaviour that becomes stiffer than Hertz with roughness and after about 4 N the gradient of the curve is closer to that of Hertz.

If cycles of load are carried out at moderate loads and on stronger particles such as quartz, then on unloading there is generally only a small amount of plastic displacement evident (Figure 7). At about 2 μm this plastic deformation is considerably larger than could be accounted for by asperity flattening. Tests on slightly larger Leighton Buzzard sand particles of mean diameter 2.36 mm were carried out by Yao et al. (2022) in particle to platen tests. Interferometry profiles by Yao et al. (2022) of a typical particle in Figure 8 clearly show extensive plastic deformations in the vicinity of the contact and in fact up to 80 N the roughness only reduced by around 10% from an initial value of about 0.416 μm so the asperity flattening contribution to the plastic displacements was small. In contrast for the weaker carbonate particles even before overall particle breakage there was significant fracture damage at the contact, giving an irregular loading curve and irrecoverable displacements that are an order of magnitude larger (Figure 7).

For the granite ballast, Hertz deviates from the data much more than for the sands because of the high roughness (Figure 9). The prediction is shown for a mean contact radius of 2 mm and E = 70 GPa for granite (Vasconcelos et al., 2008; Domede et al., 2019). Hertz with roughness (labelled Hertz*) still fits the data well, but unlike the sands unload-reload data from test SC15 indicate very large plastic displacements, which in this case would be consistent with plasticity within the asperities since S_q = 18.2 μm. So although an elastic model such as that of Greenwood et al. (1984) / Yimsiri & Soga (2000) fits the data well, it cannot capture this plasticity and the unloading is better modelled by Hertz.

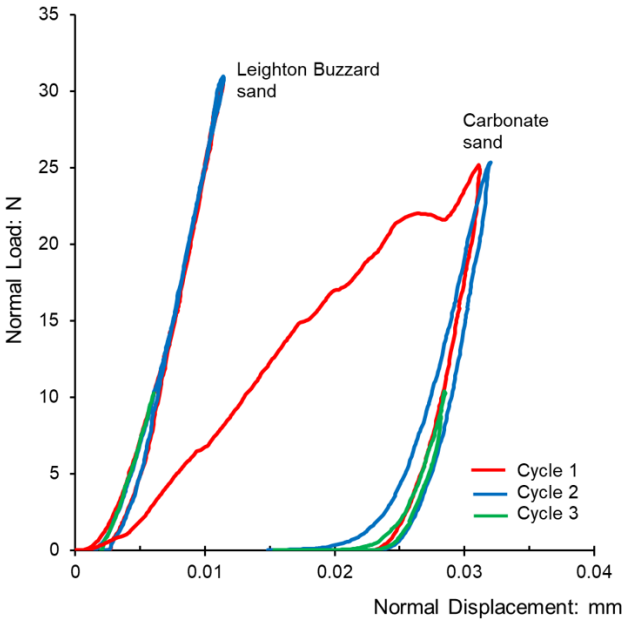

Figure 7. Cyclic normal loading of Leighton Buzzard and Carbonate sand particles (data from Nardelli & Coop, 2016 and 2019).

4. Tangential loading

Typical tangential loading data for a variety of sands of diameters 1.18−2.36 mm are shown in Figure 10a. Just as for normal loading there is considerable scatter, partly arising from different diameters, partly the different mineralogies and hence different Young's moduli, but also from the various different coefficients of inter-particle friction of the sands, μ, that control the shear stress at

sliding failure. Some scatter is also undoubtedly caused by local variations in the contact geometry that cannot be observed from external microscope observation but would need nano-X ray CT to resolve. For the granite ballast in Figure 10b the tangential loads T have been normalised by the normal load N and also by μ so that each curve tends to unity at large displacements.

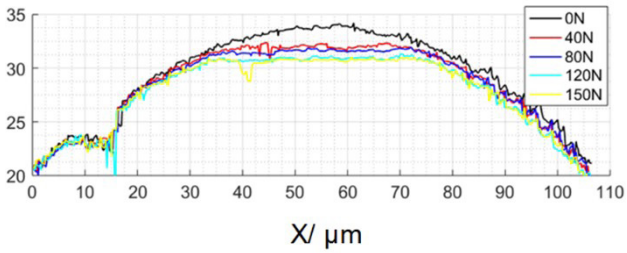

Figure 8. Contact deformation of a Leighton Buzzard sand particle (after Yao et al., 2022).

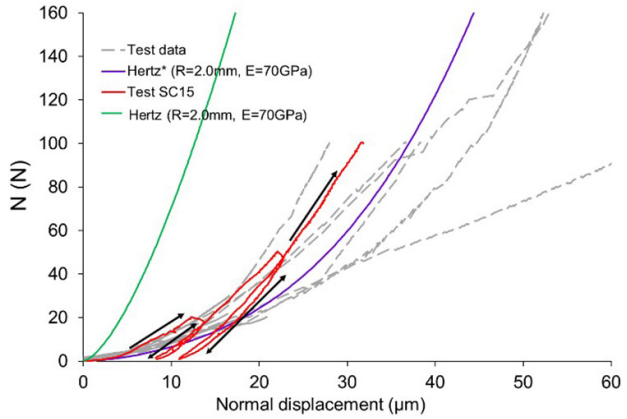

Figure 9. Normal loading test data for granite ballast (modified from Wong & Coop, 2023; Hertz* is Hertz with roughness).

Stiffnesses may be derived from the force-displacement plots by taking local tangents calculated by regression over a short interval of the data points. These are given in Figure 11 for the data from Figure 10. In each case these are highly non-linear tending towards constant values at very small displacements less than around 1 μm and to zero at sliding failure which can occur at any displacement from a few microns to a few hundred microns depending on the particles. Apart from the nature and geometry of the particles the load level has a clear effect, as seen in Figure11b for the ballast, and the large difference of stiffness between the ballast and sand particles is mostly a function of the higher load levels because the contact radii are not so different, even if the particle sizes are.

Simple predictions for tangential stiffness may be made from Mindlin & Deresiewicz (1953), who derived the initial elastic tangential stiffness, K_{T0} as:

$$K_{T0} = 8a_H \left(\frac{2-\nu_1}{G_1} + \frac{2-\nu_2}{G_2} \right)^{-1} \tag{4}$$

where G_1 and G_2 are the shear moduli of the two contacting materials. Their derivation is an extension of Hertz and so assumes elastic smooth spheres. The decay of stiffness K_T with displacement is then hysteretic and empirical and the equation used depends on the direction of loading and the load T^* at the last turning point:

(a) (b)

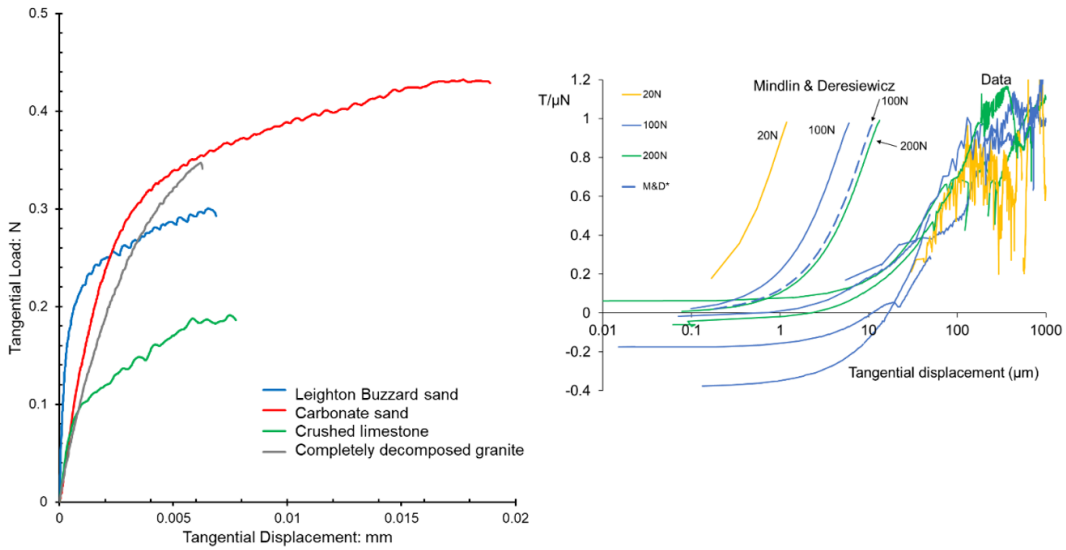

Figure 10. Tangential loading tests: (a) various sands at 1 N normal load (diameters 1.18−2.36 mm, using data from Nardelli & Coop, 2019); (b) granite ballast (modified from Wong & Coop, 2023; M&D* with roughness).

$$T \text{ increasing, } |T| \le |T^*| K_T = K_{T0}\left(1-\frac{T-T^*}{2\mu N}\right)^{1/3} \quad (5)$$

$$T \text{ increasing, } |T| > |T^*| \; K_T = K_{T0}\left(1-\frac{T}{\mu N}\right)^{1/3} \quad (6)$$

$$T \text{ decreasing, } |T| \le |T^*| \; K_T = K_{T0}\left(1-\frac{T^*-T}{2\mu N}\right)^{1/3} \quad (7)$$

$$T \text{ decreasing, } |T| > |T^*| \; K_T = K_{T0}\left(1+\frac{T}{\mu N}\right)^{1/3} \quad (8)$$

Comparisons between the Mindlin and Deresiewicz predictions and the data for Leighton Buzzard sand and given in Figure 12. The μ values used in the predictions were those measured for each test. For one test at 7 N normal load (Figure 12a) it is clear that the prediction is significantly too stiff. To check if the decay equation is correct, a prediction is

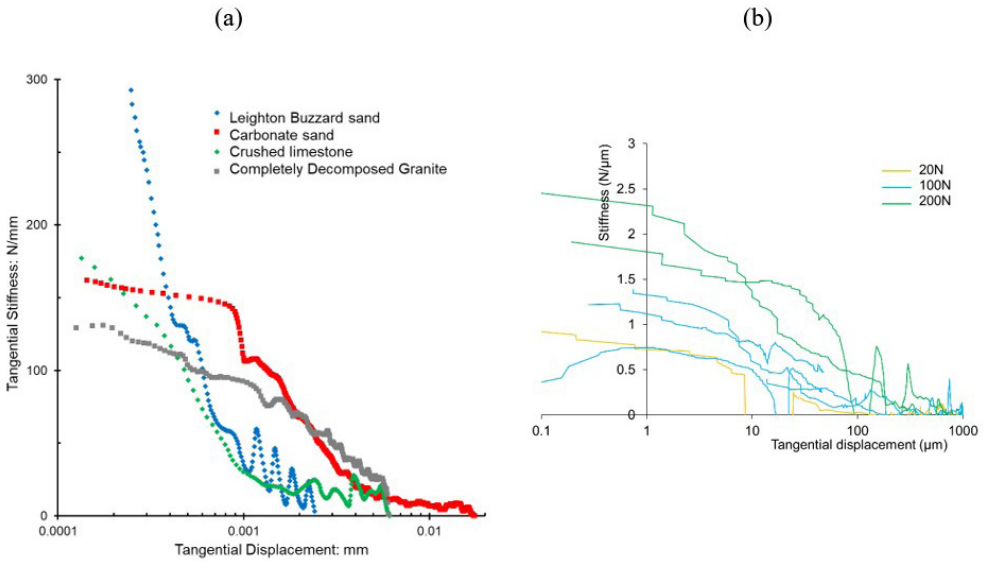

Figure 11. Tangent stiffnesses: (a) various sands at 1 N normal load (using data from Nardelli & Coop, 2019); (b) granite ballast at different normal loads (modified from Wong & Coop, 2023).

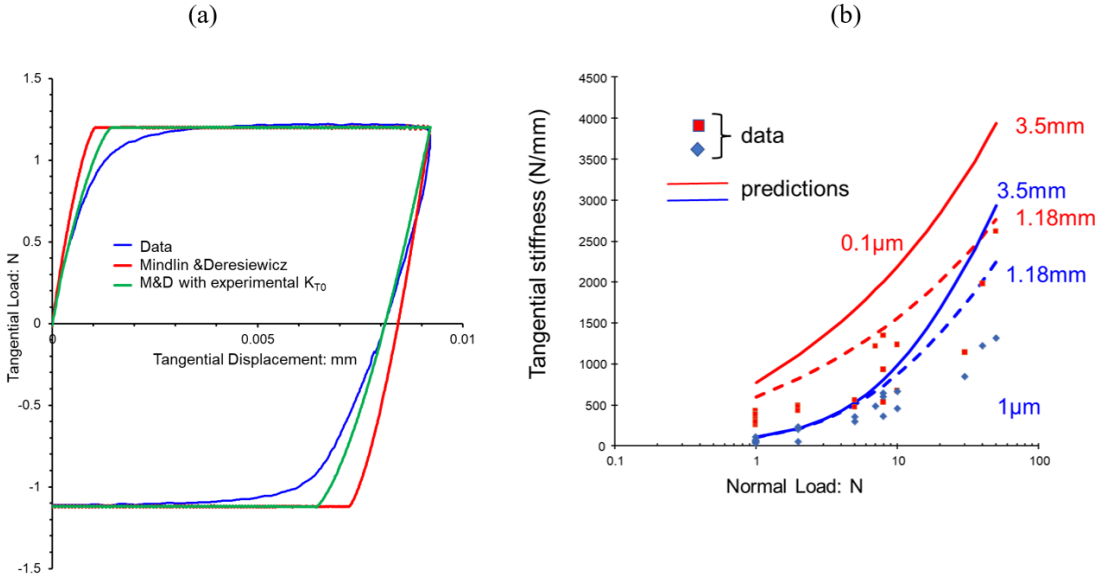

Figure 12. Mindlin and Deresiewicz predictions for Leighton Buzzard sand a) comparison of force-displacement curves at 7 N normal load, b) measured and predicted stiffnesses (modified from Nardelli & Coop, 2019).

also shown starting from the measured rather than predicted K_{T0}. The decay is then reasonably matched for the first part of the curve up to about T = 0.5 N. All of the Leighton Buzzard sand data are shown for two displacements, 0.1 and 1 μm, on Figure 12b. These are compared with Mindlin and Deresiewicz predictions for the largest and smallest particles tested which were 3 mm and 1.18 mm. The general trend of increasing stiffness with load level is matched quite well but the predictions are consistently around a factor of about two too high. In comparison the predictions for the granite ballast in Figure 10b are much worse, being over an order of magnitude, which is too stiff. For these a mean contact radius of 2 mm was used for the upper, pointed particle with an infinite radius for the lower flat one. For the ballast there is again a load level effect on stiffness as is evident in Figure 11b, but from Figure 10b it is clearly much less than predicted.

The much worse predictions for the ballast are likely to arise from the much greater particle roughness, Hertz-Mindlin assuming smooth particles. Otsubo et al. (2015) tried to account for this using the same ratio of the initial shear stiffness to the current normal stiffness at the applied normal load (K_T/K_N) for a rough surface as for smooth surfaces. The new prediction at 100 N normal load using K_N from Greenwood et al. (1984) for the ballast is labelled M&D* on Figure 10b, but the differences with the measured data remain very large. It is interesting that while Greenwood et al. (1984) is able to capture the normal loading well, its extension to tangential loading in this way is not successful.

Since there is significant plastic displacement in normal loading, it might be expected that pre-loading would affect the tangential stiffness. In Figure 13 the same pair of carbonate sand particles have been sheared tangentially at 1 N and then at 1 N after pre-loading to 10 N, which clearly has a significant effect on the stiffness decay.

Within Mindlin and Deresiewicz the decay of stiffness is assumed to result from the onset of local micro-slips within the contact area and there is no assumption of plastic deformation of the particles or their asperities. An attempt was made to examine if plastic deformation rather than simply local slipping could be shown to occur by shearing two particles of Leighton Buzzard sand around a circular force-controlled path of 0.6 N radius under a normal load of 4 N, so that the displacements were all small and much less than required for overall sliding failure (Figure 14). The displacement increment vectors at various points around the imposed force circle have some scatter because of the difficulty in resolving the tiny displacements, but generally they do not indicate any non-coaxiality that might be a symptom of, for example, plastic asperity deformations.

5. Sliding failure

Typical data for the inter-particle forces at sliding failure are very scattered, as in Figure 15a and a valuable test is then the "swipe test" in which the interface is taken to failure and then the normal force increased slowly while sliding continues, which gives a more continuous failure envelope. The values of μ are still scattered but this does confirm that for each particle pair the envelope is generally straight with a fairly constant μ, at least over a limited range of forces. To resolve the μ values for any sand therefore takes a large number of tests, but when that is done clear differences emerge between sands (Figure 15b). The Eglin sand that has been included here is a sedimentary sand with a mixed mineralogy, mostly quartz and feldspar (Nardelli et al., 2017).

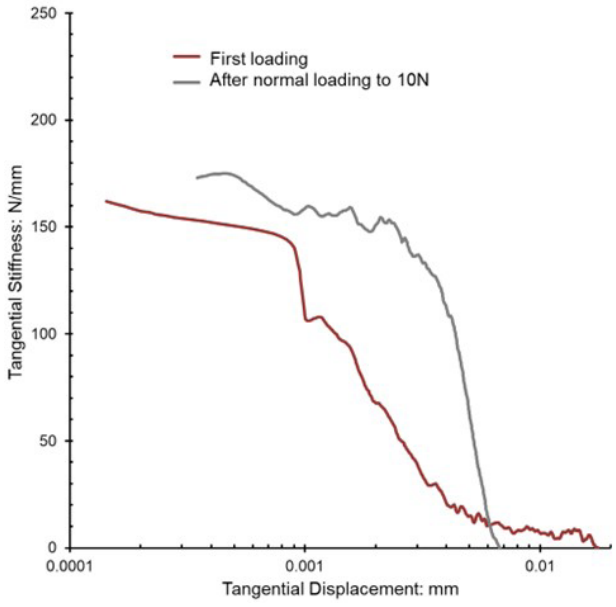

Figure 13. Effect of normal pre-loading on tangential stiffnesses for carbonate sand particles at 1 N (after Nardelli & Coop, 2019).

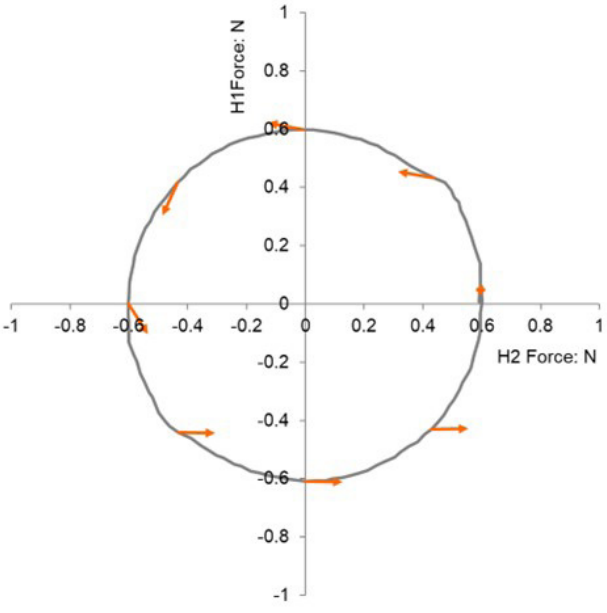

Figure 14. Displacement increment vectors for Leighton Buzzard sand under a normal load of 4 N (after Nardelli & Coop, 2019).

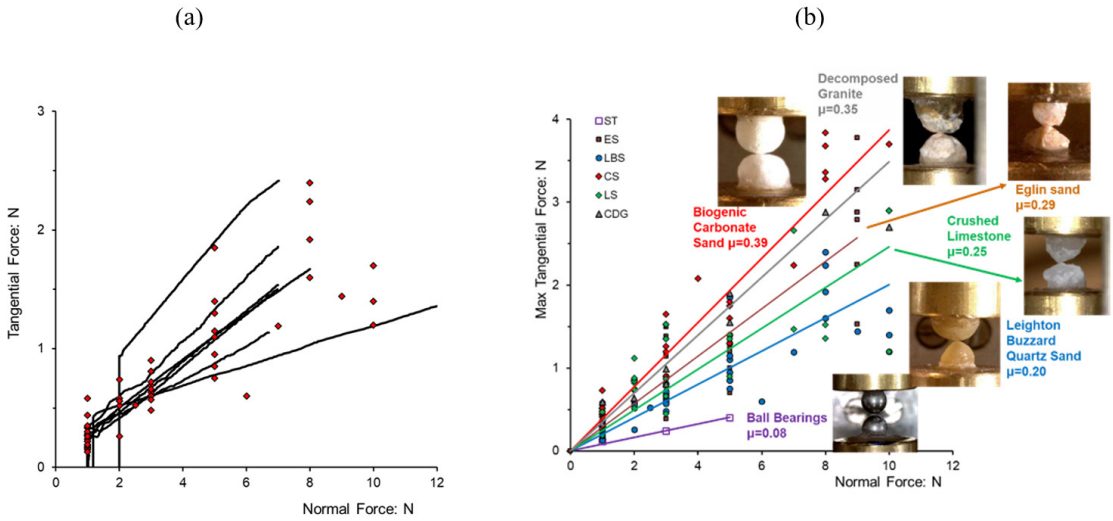

Figure 15. Frictional sliding failure envelopes: (a) Leighton Buzzard sand, data for sliding failure and "swipe" tests; (b) various sands (after Nardelli & Coop, 2019).

It is clear that shape plays little role in determining μ since the carbonate sand is one of the most rounded and most spherical but has the highest μ and Figure 16 reveals that it is the local roughness that is the controlling factor. The RMS or S_q roughnesses were measured over an area that was of the same order of magnitude as the likely particle contact area, subtracting the local shape so they would not be affected by roundness or angularity. For the sands and artificial materials this was done by white light interferometry but the much coarser roughnesses of the granite ballast were measured by a Z-stack 3D surface reconstruction using an optical microscope. The roughness of a sand will be related to its mineralogy, structure and geological history. The sedimentary Leighton Buzzard sand underwent erosion, transport and deposition and so the transportation/depositional processes in water give it its smooth surface and low μ as well as a rounded shape that will be shown below to affect strength. In contrast the decomposed granite has never undergone transport, having an origin through weathering, leading to rougher particles and hence higher μ, as well as greater angularity which reduces strength. The carbonate sand also had a sedimentary origin in water but the cellular structure of the coral probably gives rise to its greater roughness.

Wear of the particle contacts results in a change of μ. For the granite ballast 2 mm cycles were carried out between the nominal point and nominal flat contacts after an initial linear shear from the starting point at zero displacement to +1 mm. The linear shear μ values are given as cycle 1. There is a very rapid increase of μ for the first few full cycles after which the increase slowed, typically tending to stabilise after a few hundred cycles. The cycling gave rise to a large degree of grinding with a powder produced at the contact. However, even if the roughness, which started high, tended to reduce, μ increased (Figure 17). This occurred even when the ground powder was removed. The values of μ in Figure 17b were average

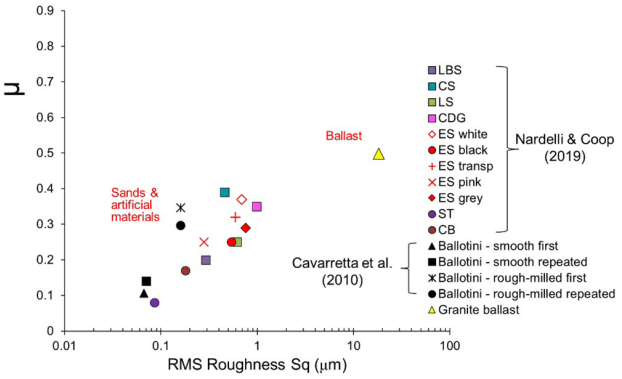

Figure 16. Influence of particle roughness on coefficient of inter-particle friction (modified from Wong & Coop, 2023, and Nardelli & Coop, 2019).

values taken in the middle section of the force-displacement curves, a selection of which are given in Figure 17a. As grinding continued the other effect is to excavate a cavity in the flat particle giving mechanical interlock and increased resistance as the corners of the travel are reached. On Figure 17b the mean values for tests at the three load levels used indicate no effect of the normal force N on μ even if for monotonic tests Nardelli & Coop (2019) seemed to observe a small μ reduction for high N on the quartz sand.

6. Particle strength

Following the localised damage that may occur at contacts (Figure 7), continued normal loading will lead eventually to catastrophic failure. This was examined using high speed imaging by Wang & Coop (2016) using the apparatus in Figure 4. The single particle strength data in

Figure 18a for particle size 1.18−2.36 mm were calculated as $0.9N/(d_2 \times d_3)$ where d_2 and d_3 are the intermediate and minimum diameters. Two predominant modes of failure were identified, a slow splitting from platen to platen and a violent explosive type, although there were variants on these two, notably failures through progressive chipping. The particles that failed explosively were the minority at about 34% but were stronger.

A local roundness at the particle-platen contact was defined as r_c/R_{ins} where r_c is the local radius of particle curvature at the contact and R_{ins} is the radius of the largest inscribed circle within the vertical particle outline. The minimum of the values for the two contacts was used, generally the top one. The effect on the strength is clear in Figure 19 for both the quartzitic Leighton Buzzard sand and the much weaker weathered particles of a decomposed granite. The more angular particles tended to have lower strengths because the stress concentrations at the platen contacts promoted splitting while a more rounded shape allowed greater stored energy and a more even stress distribution so that failure was sudden and explosive. The overall sphericity of the particles had no effect on strength.

Loading the particles to failure between two points rather than platens ensured that a splitting mode of failure was achieved every time and gave the same strength as the splitting mode for platen loaded particles (Figure 20). Point load tests are therefore more consistent, but the question remains about which strength is more relevant to soil particles in a matrix of others.

In an attempt to examine strengths under conditions better resembling those in an assembly of grains, Todisco et al.

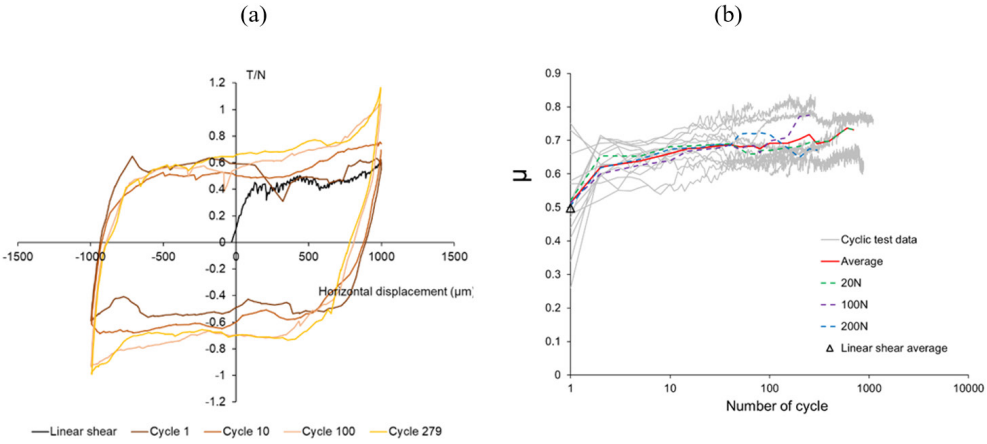

Figure 17. The development of inter-particle friction of granite ballast with wear (after Wong & Coop, 2023).

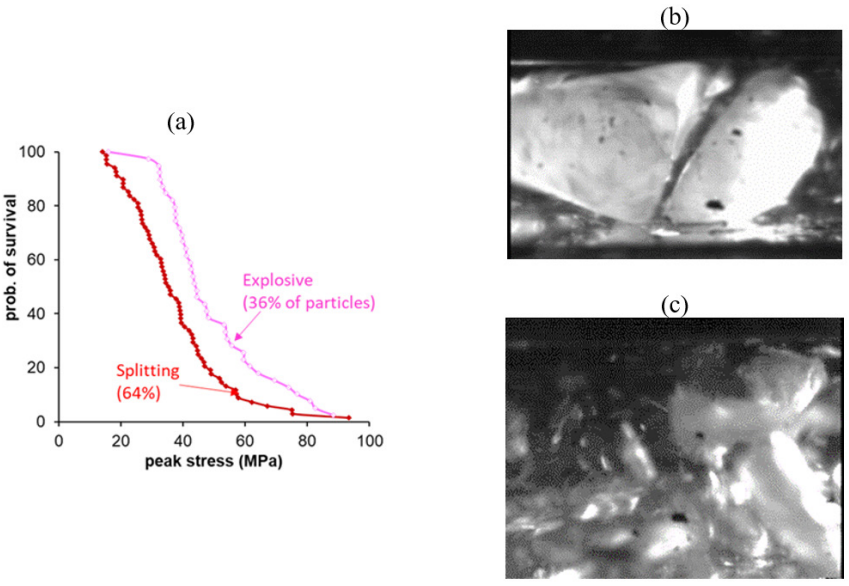

Figure 18. The interaction of mode of failure and strength for 1.18−2.36mm particles: (a) peak stress data; (b) example of a splitting mode; (c) example of an explosive mode (after Wang & Coop, 2016).

(2017) used the arrangement shown in the schematic of Figure 21, in which the crushed particle was between three support particles at both the base and top giving a coordination number *CN* of 6. Other tests used one contact particle at the top so *CN* = 4. The effect of coordination number is clear. The platen test strengths plotted between the *CN* = 4 and 6 data, but given the complexity of the loading of the platen loading test this is not surprising. A platen loading test is unusual in that anything other than a perfect sphere will generally have three contacts at the base of the particle and one at the top at the start of the test, so *CN* = 4. The nature of the contacts is also flat to curved surface rather that curved to curved as it would be in the assembly.

It is often assumed that particles fracture on diametric planes between the platen contacts, but close examination of fractured particles of the Leighton Buzzard sand (Figure 22) shows that actually quartz, which has no cleavage, fractures on conchoidal surfaces. This image was taken by Zhao et al. (2015) who carried out single particle crushing tests in a micro X-ray CT. It is commonly assumed that larger sand particles are weaker by virtue of having a greater probability of containing larger flaws, but in Figure 22 there are practically no flaws visible and so this seems an unlikely explanation. Flaws would not indeed be expected in quartz that typically has its origin in a crystalline igneous rock. Cavarretta et al. (2017) demonstrated that a more consistent reason for the apparent size effect is that, as is also shown in Figure 19, a flatter relative curvature between the platen and particle gives higher strengths, and naturally that curvature depends on particle size.

The quartz particles of Leighton Buzzard sand therefore derive their high strength not only from the solid quartz mineralogy but also their rounded shape, while a decomposed granite has a much lower particle strength, as in Figure 19, which is mostly caused by its weak internal structure derived from its origin through weathering of a mixed mineralogy crystalline rock. Figure 23 shows the typical failure pattern of one particle. The particle is mostly of quartz and feldspar but also evident are faint lines that probably indicate pre-existing fissures relating to the stresses induced by weathering. Upon breakage, three types of fracture may be seen. Some run along

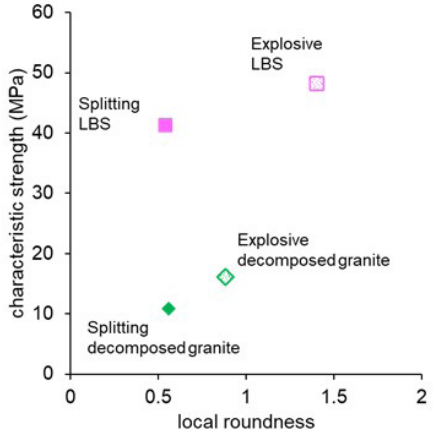

Figure 19. Failure strengths for 1.18−2.36 mm particles of Leighton Buzzard sand and decomposed granite (modified from Wang & Coop, 2016).

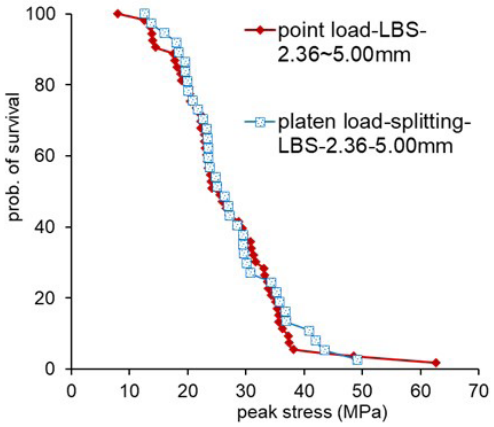

Figure 20. Failure strengths for 2.36−5.00 mm particles of Leighton Buzzard sand in platen loading and point loading tests (after Wang & Coop, 2018).

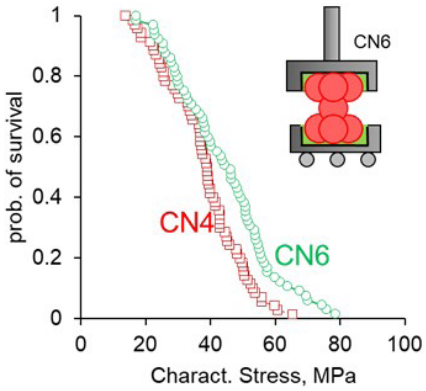

Figure 21. Multiple contact particle crushing tests for Leighton Buzzard sand (2−2.6 mm diameter). (Modified from Todisco et al., 2017).

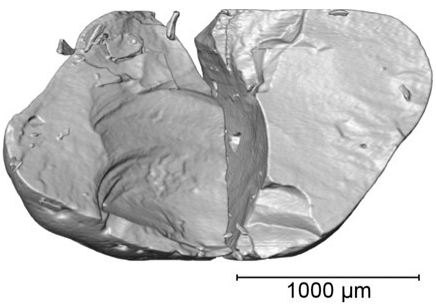

Figure 22. Fracture patterns of a typical Leighton Buzzard sand particle (after Zhao et al., 2015).

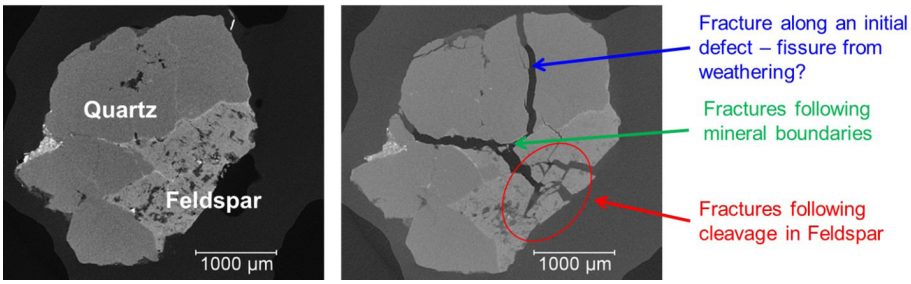

Figure 23. Fracture patterns in a highly decomposed granite particle (modified from Zhao et al., 2015).

these pre-existing planes of weakness in the quartz. In the feldspar the fractures tend to follow a grid intersecting at very roughly 90° which corresponds to the cleavage of the feldspar. Other fractures follow the mineral boundary between quartz and feldspar. The internal structure can therefore play a central role in the strength of sand particles.

7. Influence of fluid immersion

For the granite ballast the influence of the presence or absence of water on the normal contact stiffness was investigated by flooding the contact during normal loading. In Figure 24 there is clearly no effect, and this was also the case for tangential loading. The lack of any effect on the contact stiffnesses was reflected at the meso-scale by triaxial samples having the same small strain stiffness when saturated or dry (Altuhafi & Coop, 2023).

However, at sliding failure there was a substantial influence of water lubrication (Figure 25). While the water inundated contacts start with similar μ values to the dry, they tend to reduce rather than increase with cycling. One test was dried during shearing and one wetted, and the change of μ was immediate for either. The data points indicate where the interface was cleaned of the ground powder for some tests. Since this was done with water it also resulted in a temporary reduction in μ. Nardelli & Coop (2019) found no influence of water immersion for any of the sands that they tested. Possibly the difference of response for the ballast is related to its much greater roughness.

In contrast, immersion in oil does affect the inter-particle angle of friction (=$\tan^{-1}\mu$) for Leighton Buzzard sand (Figure 26).

While water can adversely affect the particle strength of some sands and rocks (e.g. Coop & Lee, 1995; Oldecop & Alonso, 2001) it typically does not affect the strength of quartz sands (Figure 27). However, immersion in glycerine did increase the particle strength considerably and this corresponded to greater stiffness and less particle breakage in oedometer tests.

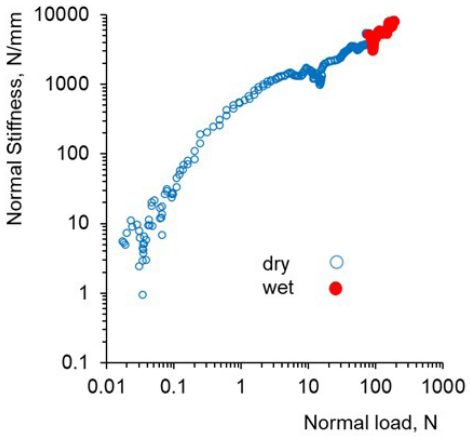

Figure 24. The effect of water inundation on the stiffness in normal loading of a granite ballast (after Altuhafi & Coop, 2023).

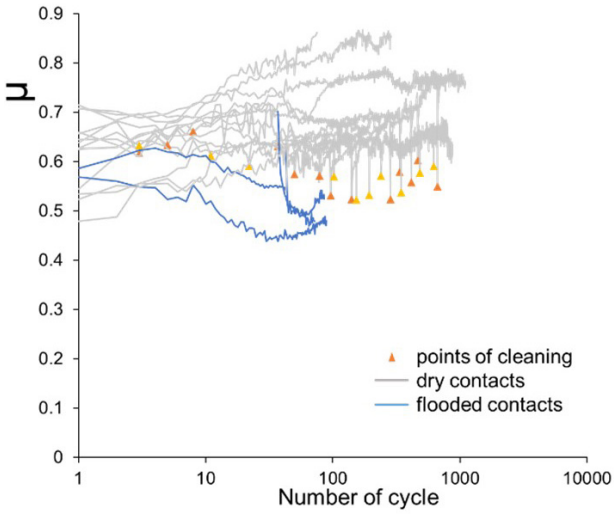

Figure 25. The effect of water inundation on μ during shear cycles on granite ballast (modified from Wong & Coop, 2020).

8. Rate effects and creep

Since creep and rate effects influence the mechanics of sands at the meso-scale we should also expect to see them at the micro-scale. Figure 28a shows creep data for a granite ballast contact; the creep stabilises after a couple of days.

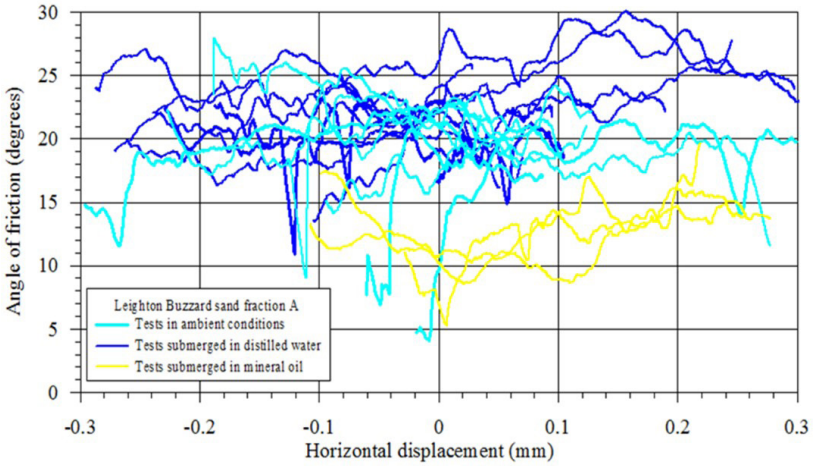

Figure 26. The influence of water and oil immersion on the inter-particle angle of friction between Leighton Buzzard sand particles (after Cavarretta et al., 2011).

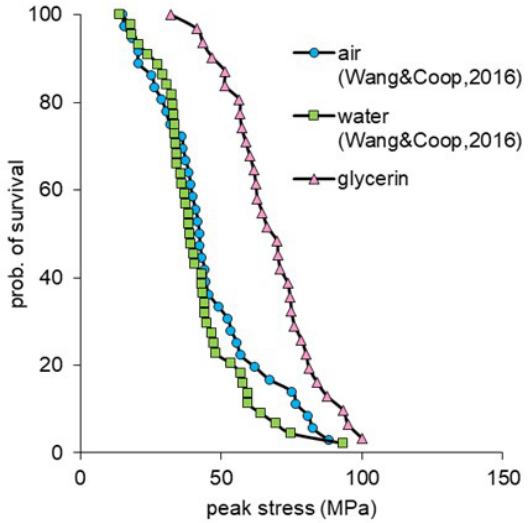

Figure 27. The effects of immersion in water and glycerine on strength of Leighton Buzzard sand particles (1 .18−2.36 mm). (After Wang et al., 2023).

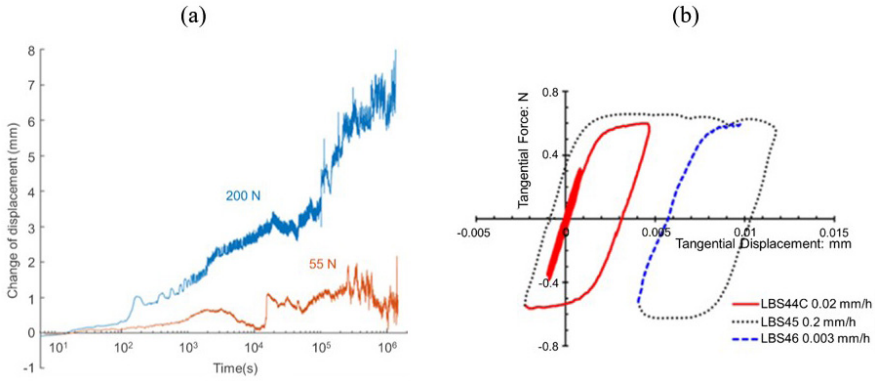

Figure 28. (a) creep under two normal loads of a point to flat granite ballast contact (after Wong & Coop, 2023); (b) influence of displacement rate on sliding shearing of Leighton Buzzard sand (after Nardelli & Coop, 2019).

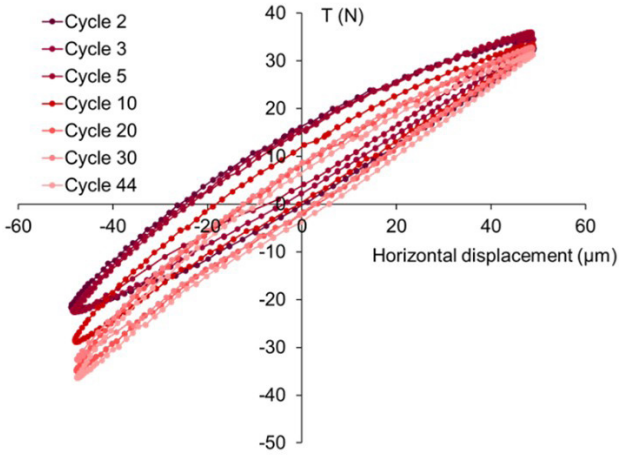

Figure 29. Pre-sliding tangential loading cycles of granite ballast (after Wong & Coop, 2023).

The amount of creep (or more correctly contact ageing) was dependent on the normal load and was exacerbated by the addition of a tangential load. Similar data were observed for a quartz sand by Michalowski et al. (2018) but at much smaller loads. While some authors have found rate of sliding effects in sand (Kasyap & Senetakis, 2019) over almost two orders of magnitude of rate of displacement there was no significant effect for the Leighton Buzzard sand (Figure 28b) or for the granite ballast (Wong & Coop, 2023).

9. Pre-failure cyclic loading

Typical data for pre-sliding cyclic tangential loading are shown in Figure 29 for the granite ballast. As the cycles continue the secant stiffness tends to increase but the loop area decrease, both tending to stabilise after around 20 cycles. The behaviour of the Leighton Buzzard sand was very similar (Nardelli & Coop, 2019). Similar behaviour was also seen in normal loading, although the stiffness tended to reduce slightly.

10. Conclusions

As computing power increases and the possibility to model soils with digital twins becomes more realistic, we will increasingly face the choice, at least for coarser graded soils, whether we continue with the rabbit hole of ever more complex continuum mechanics approaches or if we should adopt discrete ones. A correct digital twin on Avatar soil will need us to model accurately the particle shapes and contact fabric, which we can already do, and the key missing link is a thorough understanding of the contact mechanics up to and including particle damage and crushing. This requires us to jettison our beloved triaxial apparatus and develop new equipment for discrete tests on single particles.

Research on contact mechanics to date has highlighted the complexity of the response and the inadequacy of common current models to capture that behaviour. Important challenges for the future will be how we model efficiently the plasticity and damage at the particle contacts that is clearly an important feature of the behaviour, since this will necessitate that the model retains a memory of what has previously happened at a particular location on a particle. Large-scale particle damage and the mechanisms by which real geological particles fail are also key areas for future investigation and modelling.

Developing similar apparatus to those shown here for silts may well be possible, but for clays it is unlikely, so it is interesting to ponder whether in twenty years we will see a division in approaches for clastic and plastic soils and whether we will have laboratories full of inter-particle apparatus.

Acknowledgements

I would like to express my sincere thanks to Dr Vincenzo Nardelli, Dr Cacin Wong, Dr Kris Wang, Dr Fatin Altuhafi and Professor Béatrice Baudet who each helped enormously with the preparation of this paper. The work was partly funded by EPSRC grants No. EP/S026460/1 and EP/W000563/1.

Declaration of interest

The author has no conflicts of interest to declare and there is no financial interest to report.

Data availability

The datasets generated analyzed in the course of the current study are available from the corresponding author upon request.

List of symbols and abbreviations

a_H	Radius of the contact area for Hertz
a^*	Apparent area of the contact between two rough surfaces
r_c	Local contact radius
CN	Coordination number
E	Young's modulus
E^*	Equivalent Young's modulus
G	Shear modulus
K_N	Normal stiffness
K_T	Tangential stiffness
K_{T0}	Elastic tangential stiffness
N	Normal load
R	Equivalent radius at contact
R_{ins}	Radius of the largest inscribed circle within particle outline
S_q	RMS roughness
T	Tangential load
T^*	Tangential load at last force reversal
α	Normalised roughness

δ Mutual approach of contacting spheres
μ Inter-particle coefficient of friction
ν Poisson's ratios
σ Combined roughness

References

Ahmed, S., Harkness, J., Le Pen, L., Powrie, W., & Zervos, A. (2016). Numerical modelling of railway ballast at the particle scale. *International Journal for Numerical and Analytical Methods in Geomechanics*, 40(5), 713-773. http://dx.doi.org/10.1002/nag.2424.

Altuhafi, F.N., & Coop, M.R. (2023). The small strain stiffness of a railway ballast. *Géotechnique*. Ahead of print. https://doi.org/10.1680/jgeot.22.00356.

Bandini, V., & Coop, M.R. (2011). The influence of particle breakage on the location of the critical state line of sands. *Soil and Foundation*, 51(4), 591-600. http://dx.doi.org/10.3208/sandf.51.591.

Carrera, A., Coop, M.R., & Lancellotta, R. (2011). The influence of grading on the mechanical behaviour of Stava tailings. *Geotechnique*, 61(11), 935-946. http://dx.doi.org/10.1680/geot.9.P.009.

Cavarretta, I., O'Sullivan, C., & Coop, M.R. (2017). The relevance of roundness to the crushing strength of granular materials. *Geotechnique*, 67(4), 301-312. http://dx.doi.org/10.1680/jgeot.15.P.226.

Cavarretta, I., Rocchi, I., & Coop, M.R. (2011). A new inter-particle friction apparatus for granular materials. *Canadian Geotechnical Journal*, 48(12), 1829-1840. http://dx.doi.org/10.1139/t11-077.

Cole, D.M. (2015). Laboratory observations of frictional sliding of individual contacts in geologic materials. *Granular Matter*, 17(1), 95-110. http://dx.doi.org/10.1007/s10035-014-0526-0.

Cole, D.M., Mathisen, L.U., Hopkins, M.A., & Knapp, B.R. (2010). Normal and sliding contact experiments on gneiss. *Granular Matter*, 12(1), 69-86. http://dx.doi.org/10.1007/s10035-010-0165-z.

Coop, M.R., & Lee, I.K. (1993). The behaviour of granular soils at elevated stresses. In *Predictive Soil Mechanics* (pp. 200-208). London: Thomas Telford.

Coop, M.R., & Lee, I.K. (1995). The influence of pore water on the mechanics of granular soils. In *XI European Conference on Soil Mechanics and Foundation Engineering* (pp. 63-73.). Copenhagen: CRC Press.

Coop, M.R., Sorensen, K.K., Bodas Freitas, T., & Georgoutsos, G. (2004). Particle breakage during shearing of a carbonate sand. *Geotechnique*, 54(3), 157-163. http://dx.doi.org/10.1680/geot.2004.54.3.157.

Cuccovillo, T., & Coop, M.R. (1999). On the mechanics of structured sands. *Geotechnique*, 49(6), 741-760. http://dx.doi.org/10.1680/geot.1999.49.6.741.

Domede, N., Parent, T., & Sellier, A. (2019). Mechanical behaviour of granite: a compilation, analysis and correlation of data from around the world. *European Journal of Environmental and Civil Engineering*, 23(2), 193-211. http://dx.doi.org/10.1080/19648189.2016.1275984.

Fellerec, J., & McDowell, G. (2010). Modelling realistic shape and particle inertia in DEM. *Geotechnique*, 60(3), 227-232. http://dx.doi.org/10.1680/geot.9.T.015.

Greenwood, J.A., Johnson, K.L., & Matsubara, E. (1984). A surface roughness parameter in Hertz contact. *Wear*, 100, 1-3, 47-57. http://dx.doi.org/10.1016/0043-1648(84)90005-X.

Hertz, H. (1882). Ueber die Berührung fester elastischer Körper. *Journal für die Reine und Angewandte Mathematik*, 92, 156-171. http://dx.doi.org/10.1515/crll.1882.92.156.

Horn, H.M., & Deere, M.S. (1962). Frictional characteristics of minerals. *Geotechnique*, 12(4), 319-335. http://dx.doi.org/10.1680/geot.1962.12.4.319.

Jaeger, J.C., Cook, N.G.W., & Zimmerman, R. (2007). *Fundamentals of rock mechanics* (4th ed.). Malden: Wiley-Blackwell.

Jiang, M.J., Sun, Y.G., Li, L.Q., & Zhu, H.H. (2012). Contact behavior of idealized granules bonded in two different interparticle distances: an experimental investigation. *Mechanics of Materials*, 55, 1-15. http://dx.doi.org/10.1016/j.mechmat.2012.06.015.

Jovicic, V., & Coop, M.R. (1997). Stiffness of coarse-grained soils at small strains. *Géotechnique* 47(3), 545-561. Jovicic, V., & Coop, M.R. (1997). Stiffness of coarse-grained soils at small strains. *Geotechnique*, 47(3), 545-561. http://dx.doi.org/10.1680/geot.1997.47.3.545.

Kasyap, S.S., & Senetakis, K. (2019). Experimental investigation of the coupled influence of rate of loading and contact time on the frictional behavior of quartz grain interfaces under varying normal load. *International Journal of Geomechanics*, 19(10), 04019112. http://dx.doi.org/10.1061/(ASCE)GM.1943-5622.0001493.

Krumbein, W.C., & Sloss, L.L. (1963). *Stratigraphy and sedimentation.* San Francisco: W. H. Freeman and Company.

Mavko, G., Mukerji, T., & Dvorkin, J. (1998). *The rock physics handbook: tools for seismic analysis in porous media*. Cambridge: Cambridge University Press.

Michalowski, R.L., Wang, Z., & Nadukuru, S.S. (2018). Maturing of contacts and ageing of silica sand. *Geotechnique*, 68(2), 133-145. http://dx.doi.org/10.1680/jgeot.16.P.321.

Mindlin, R.D., & Deresiewicz, H. (1953). Elastic spheres in contact under varying oblique forces. Trans. *ASME. Journal of Applied Mechanics*, 20(3), 327-343. http://dx.doi.org/10.1115/1.4010702.

Muir Wood, D. (2008). Critical states and soil modelling. In *4th International Symposium on Deformation Characteristics of Geomaterials* (Vol. 1, pp. 51-72.). Atlanta: IOS.

Nakata, Y., Hyde, A.F.L., Hyodo, M., & Murata, H. (1999). A probabilistic approach to sand crushing in the triaxial test. *Geotechnique*, 49(5), 567-583. http://dx.doi.org/10.1680/geot.1999.49.5.567.

Nardelli, V., & Coop, M.R. (2016). The micromechanical behaviour of a biogenic carbonate sand. *Procedia*

Engineering, 158, 39-44. http://dx.doi.org/10.1016/j.proeng.2016.08.402.

Nardelli, V., & Coop, M.R. (2019). The experimental contact behaviour of natural sands: normal and tangential loading. *Geotechnique*, 69(8), 672-686. http://dx.doi.org/10.1680/jgeot.17.P.167.

Nardelli, V., Coop, M.R., Andrade, J.E., & Paccagnella, F. (2017). An experimental investigation of the micromechanics of Eglin sand. *Powder Technology*, 312, 166-174. http://dx.doi.org/10.1016/j.powtec.2017.02.009.

Oldecop, L.A., & Alonso, E.E. (2001). A model for rockfill compressibility. *Geotechnique*, 51(2), 127-139. http://dx.doi.org/10.1680/geot.2001.51.2.127.

Otsubo, M., O'Sullivan, C., Sim, W.W., & Ibraim, E. (2015). Quantitative assessment of the influence of surface roughness on soil stiffness. *Geotechnique*, 65(8), 694-700. http://dx.doi.org/10.1680/geot.14.T.028.

Pestana, J.M., & Whittle, A.J. (1995). A compression model for cohesionless soils. *Geotechnique*, 45(4), 611-631. http://dx.doi.org/10.1680/geot.1995.45.4.611.

Procter, D.C., & Barton, R.R. (1974). Measurements of the angle of interparticle friction. *Geotechnique*, 24(4), 581-604. http://dx.doi.org/10.1680/geot.1974.24.4.581.

Skinner, A.E. (1969). A note on the influence of interparticle friction on shearing strength of a random assembly of spherical particles. *Geotechnique*, 19(1), 150-157. http://dx.doi.org/10.1680/geot.1969.19.1.150.

Todisco, M.C., & Coop, M.R. (2019). Quantifying "transitional" soil behaviour. *Soil and Foundation*, 59(6), 2070-2082. http://dx.doi.org/10.1016/j.sandf.2019.11.014.

Todisco, M.C., Wang, W., Coop, M.R., & Senetakis, K. (2017). Multiple contact compression tests in particles crushing. *Soil and Foundation*, 57(1), 126-140. http://dx.doi.org/10.1016/j.sandf.2017.01.009.

Vasconcelos, G., Lourenço, P.B., Alves, C.A.S., & Pamplona, J. (2008). Ultrasonic evaluation of the physical and mechanical properties of granites. *Ultrasonics*, 48(5), 453-466. http://dx.doi.org/10.1016/j.ultras.2008.03.008.

Verdugo, R., & Ishihara, K. (1996). The steady state of sandy soils. *Soil and Foundation*, 36(2), 81-91. http://dx.doi.org/10.3208/sandf.36.2_81.

Wang, W., & Coop, M.R. (2016). An investigation of breakage behaviour of single sand particles using a high-speed microscope camera. *Geotechnique*, 66(12), 984-998. http://dx.doi.org/10.1680/jgeot.15.P.247.

Wang, W., & Coop, M.R. (2018). Breakage behaviour of sand particles in point load compression. *Géotechnique Letters*, 8(1), 61-65. http://dx.doi.org/10.1680/jgele.17.00155.

Wang, W., Coop, M.R., & Senetakis, K. (2019). The development of a micro-mechanical apparatus applying combined normal-shear-bending forces to natural sand grains with artificial bonds. *Geotechnical Testing Journal*, 42(2), 1090-1099. http://dx.doi.org/10.1520/GTJ20170453.

Wang, W., Degao, C., Coop, M.R., & Bingxiang, Y. (2023). Experimental study of the micro and macro scale compression behavior of a sand immersed in a viscous liquid. *Géotechnique Letters*, 13(2), 91-96. http://dx.doi.org/10.1680/jgele.22.00132.

Wong, C.P.Y., & Coop, M.R. (2020). Development of inter-particle friction in a railway ballast. *Géotechnique Letters*, 10(4), 535-541. http://dx.doi.org/10.1680/jgeot.22.00190.

Wong, C.P.Y., & Coop, M.R. (2023). The Contact Mechanics of a UK railway ballast. *Géotechnique*. Ahead of print. https://doi.org/10.1680/jgeot.22.00190.

Yao, T., Baudet, B.A., & Lourenço, S.D.N. (2022). Evolution of surface roughness of single sand grains with normal loading. *Geotechnique*, 72(6), 543-555. http://dx.doi.org/10.1680/jgeot.20.P.310.

Yimsiri, S., & Soga, K. (2000). Micromechanics-based stress-strain behaviour of soils at small strains. *Geotechnique*, 50(5), 559-571. http://dx.doi.org/10.1680/geot.2000.50.5.559.

Zhai, C., Herbold, E.B., Hall, S.A., & Hurley, R.C. (2019). Particle rotations and energy dissipation during mechanical compression of granular materials. *Journal of the Mechanics and Physics of Solids*, 129, 19-38. http://dx.doi.org/10.1016/j.jmps.2019.04.018.

Zhao, B., Wang, J., Coop, M.R., Viggiani, G., & Jiang, M. (2015). An investigation of single sand particle fracture using X-ray micro-tomography. *Geotechnique*, 65(8), 625-641. http://dx.doi.org/10.1680/geot.4.P.157.